Diurnal cycle of convection, clouds, and water vapor in the tropical upper troposphere: Satellites versus a general circulation model

Baijun Tian

Atmospheric and Oceanic Sciences Program, Princeton University, Princeton, New Jersey, USA

Brian J. Soden

NOAA Geophysical Fluid Dynamics Laboratory, Princeton, New Jersey, USA

Xiangqian Wu

NOAA/NESDIS Office of Research and Application, Camp Springs, Maryland, USA

[1]   Global high-resolution (3-hourly, $0.1° \times 0.1°$ longitude-latitude) water vapor (6.7 μm) and window (11 μm) radiances from multiple geostationary satellites are used to document the diurnal cycle of upper tropospheric relative humidity (UTH) and its relationship to deep convection and high clouds in the whole tropics and to evaluate the ability of the new Geophysical Fluid Dynamics Laboratory (GFDL) global atmosphere and land model (AM2/LM2) to simulate these diurnal variations. Similar to the diurnal cycle of deep convection and high clouds, coherent diurnal variations in UTH are also observed over the deep convective regions, where the daily mean UTH is high. In addition, the diurnal cycle in UTH also features a land-sea contrast: stronger over land but weaker over ocean. UTH tends to peak around midnight over ocean in contrast to 0300 LST over land. Furthermore, UTH is observed to lag high cloud cover by ∼6 hours, and the latter further lags deep convection, implying that deep convection serves to moisten the upper troposphere through the evaporation of the cirrus anvil clouds generated by deep convection. Compared to the satellite observations, AM2/LM2 can roughly capture the diurnal phases of deep convection, high cloud cover, and UTH over land; however, the magnitudes are noticeably weaker in the model. Over the oceans the AM2/LM2 has difficulty in simulating both the diurnal phase and amplitude of these quantities. These results reveal some important deficiencies in the model's convection and cloud parameterization schemes and suggest the lack of a diurnal cycle in SST may be a shortcoming in the boundary forcing for atmospheric models.   *INDEX TERMS:* 3314 Meteorology and Atmospheric Dynamics: Convective processes; 3359 Meteorology and Atmospheric Dynamics: Radiative processes; 3360 Meteorology and Atmospheric Dynamics: Remote sensing; *KEYWORDS:* diurnal cycle, satellite radiance, GCM

1. Introduction

[2]   General circulation models (GCMs) have been powerful tools for climate studies, and tremendous effort has been expended to improve GCMs' physical parameterizations and to evaluate models' performance. Most current GCM evaluations focus on the model's climatology at monthly, seasonal and annual timescales instead of its variability (e.g., J. L. Anderson et al., The new GFDL global atmosphere and land model AM2/LM2: Evaluation with prescribed SST simulations, submitted to *Journal of Climate*, 2004, hereinafter referred to as Anderson et al., submitted manuscript, 2004). There are apparent limita-

tions to this approach because it is possible for a GCM to produce a realistic climate state for the wrong reasons. Thus it is desirable to evaluate a model's variability at various timescales, such as diurnal, intraseasonal, interannual, and decadal, against observations. Associated with well-defined, large, and external diurnal (24 hour) variations of solar forcing, the diurnal cycle is one of the fundamental modes of variability of the global climate system. It provides a large and well-documented source of forcing with frequent sampling. Thus comparisons of the diurnal cycle between observations and a GCM represent a powerful tool for evaluating the GCM performance and identifying the model's deficiencies [e.g., *Slingo et al.*, 1987; *Randall et al.*, 1991; *Lin et al.*, 2000; *Yang and Slingo*, 2001; *Betts and Jakob*, 2002; *Dai and Trenberth*, 2004; A. Slingo et al., Simulations of the diurnal cycle in

a climate model and its evaluation using data from Meteosat 7, submitted to *Quarterly Journal of the Royal Meteorological Society*, 2004, hereinafter referred to as Slingo et al., submitted manuscript, 2004].

[3] *Slingo et al.* [1987] studied the diurnal cycle of outgoing longwave radiation (OLR) simulated by the United Kingdom (UK) Meteorological Office 11-layer GCM. They demonstrated that comparisons of the diurnal cycle between models and observations have considerable potential for not only validating the cloud and other parameterization schemes used, but also for understanding the observed variations. *Randall et al.* [1991] analyzed the diurnal variability of the hydrological cycle in an earlier version of the Colorado State University GCM to investigate the causes of the diurnal cycle of precipitation over the oceans. *Lin et al.* [2000] compared the observed diurnal variability of the hydrological cycle and radiative fluxes with simulation from a recent CSU GCM and evaluated improvements and deficiencies of the model physics. *Yang and Slingo* [2001] documented the diurnal cycle in convection, cloudiness, and surface temperature using the European Union Cloud Archive User Service (CLAUS) dataset of the window (11– 12 μm) brightness temperature. Their results revealed several deficiencies in the Meteorological Office Unified Model's ability to reproduce the observed phase of the diurnal cycle in convection. *Betts and Jakob* [2002] evaluated the diurnal cycle of precipitation and surface thermodynamics and fluxes in the European Center for Medium-Range Weather Forecast (ECMWF) model using observations from the Large-scale Biosphere-Atmosphere Experiment over the Amazonia in order to evaluate the model's convection parameterization. *Dai and Trenberth* [2004] evaluated the performance of version 2 of the Community Climate System Model in simulating the diurnal cycle in surface air temperature, surface pressure, upper air winds, cloud amount and precipitation, and diagnosed the deficiencies in underlying model physics. Slingo et al. (submitted manuscript, 2004) examined the diurnal cycle in the Hadley Center climate model using simulations of the infrared (IR) radiances observed by METEOSAT-7.

[4] In addition to evaluating climate models, the diurnal cycle over the tropics is of intrinsic interest with studies dating back several decades. Most previous studies have focused on the diurnal cycle of the hydrological cycle, such as deep convection and associated precipitation [e.g., *Wallace*, 1975; *Gray and Jacobson*, 1977; *Fu et al.*, 1990; *Hendon and Woodberry*, 1993; *Janowiak et al.*, 1994; *Chen and Houze*, 1997; *Yang and Slingo*, 2001; *Dai*, 2001; *Nesbitt and Zipser*, 2003], cloudiness [e.g., *Rozendaal et al.*, 1995; *Bergman and Salby*, 1996; *Garreaud and Wallace*, 1997] and OLR [e.g., *Hartmann and Recker*, 1986; *Smith and Rutan*, 2003]. However, there are few studies of the diurnal cycle of atmospheric water vapor, which is directly associated with the hydrological cycle, partly due to the lack of high temporal- and spatial-resolution water vapor observation from traditional balloonborne radiosondes [*Elliot and Gaffen*, 1991; *Dai et al.*, 2002]. This is particularly true for upper tropospheric water vapor, which plays a particularly important role in the global climate system [*Held and Soden*,

2000]. *Dai et al.* [2002] studied the vertical structure in the diurnal cycle of atmospheric water vapor using 3-hourly radiosonde data from the Atmospheric Radiation Program (ARM) Cloud and Radiation Testbed (CART) site near Lamont, Oklahoma. They found that the atmospheric specific humidity above ∼2 km typically peaks around 0300 LST in all seasons. Near the surface, the atmospheric specific humidity is lower in the morning than in the afternoon and evening in all seasons except summer.

[5] Geostationary (GEO) satellites provide high temporal sampling of the IR radiation at the 6.7 μm channel. As shown by *Soden and Bretherton* [1993], the 6.7 μm water vapor radiance is primarily sensitive to the relative humidity averaged over a deep layer, centered in the upper troposphere (typically 200–500 hPa), and can be used to accurately infer the upper tropospheric relative humidity (UTH). Thus the 6.7 μm water vapor radiances from geostationary satellites provide a powerful data set for studying the diurnal cycle of upper tropospheric water vapor. *Udelhofen and Hartmann* [1995] provided one of the first attempts to document the diurnal cycle of UTH using four days of GOES-7 6.7 μm radiances. Using three months of hourly radiances from GOES-7, *Soden* [2000] documented the diurnal cycle in UTH, and its relationship to high-cloud cover and deep convection. *Soden* [2000] found a coherent diurnal cycle in UTH that generally peaks around midnight (1900–0200 LST), with a minimum near noon (1000–1300 LST). UTH is observed to lag the upper tropospheric cloud cover by 2 hours. The above two studies used data from only a single satellite (GOES-7), and were therefore confined to a small part of the tropics. A comprehensive analysis of the diurnal cycle of UTH over the whole tropics has not yet been performed.

[6] The purpose of this study is to document the diurnal cycle in UTH, and its relationship to deep convection and high cloud over the whole tropics (30°S–30°N) from a new data set constructed from global, high-resolution (3-hourly, 0.1° × 0.1° longitude-latitude) water vapor (6.7 μm) and window (11 μm) radiances from multiple geostationary satellites. This data set will then be used to evaluate the ability of the new Geophysical Fluid Dynamics Laboratory (GFDL) global atmosphere and land model known as AM2/LM2 (Anderson et al., submitted manuscript, 2004) to capture the observed diurnal variations. The plan for the rest of this paper is as follows: The satellite data intercalibration, UTH retrieval, model simulation, and diurnal cycle analysis method are described in section 2. Section 3 will present the main results of the observed diurnal cycle from satellites, while the GCM evaluation in terms of diurnal cycle is given in section 4. Conclusions are summarized in section 5.

2. Data and Method
2.1. Satellite Radiance and Its Intercalibration

[7] The primary data for this study are geostationary satellite IR radiances (expressed as equivalent black body temperatures, T_b) in the water vapor (6.7 μm) and window (11 μm) channels ($T_{6.7}$ and T_{11}). The data cover the year

1999 at the temporal resolution of 3 hours over the latitudes of 60°N–60°S and global longitude, at a spatial resolution of 0.1° × 0.1° longitude-latitude. These data are from the following five geostationary satellites with their spatial coverage in parentheses: GOES-10 (180°–105°W), GOES-8 (105°W–35°W), METEOSAT-7 (35°W–35°E), METEOSAT-5 (35°E–100°E), and GMS-5 (100°E–180°).

[8] Due to differences in satellite calibration and spectral responses of the channels, a procedure is necessary to intercalibrate the measurements made by these satellites. The central issue of intersatellite calibration is that, with different spectral response functions, sensors often observe different radiating targets even if they are perfectly colocated. For atmospheric channels such as the 6.7 μm water vapor channel, different sensors are sensitive to different portions (vertically) of the atmosphere. For surface channels such as the visible channel, different sensors are sensitive to different surface characteristics.

[9] In this work, we use the polar orbiting satellite NOAA-14 High Resolution IR Sounder (HIRS) that flew under all the geostationary satellites to intercalibrate the geostationary satellite measurements. Data for this inter-calibration were collected from September 1999 to January 2002, except for the METEOSAT-5 data collection that started in October 2001. The strategy is to find the measurements by the polar orbiting satellite that are concurrent and colocated with those from a geostationary satellite, study their differences, and apply that knowledge to estimate what the polar orbiting satellite would observe using measurements from that geostationary satellite. The major advantage of this approach is that it is based on samplings that best represent the measurements to be intercalibrated. This method also directly converts geostationary satellite measurements to a common standard and avoids possible uncertainty in spectral response functions.

2.1.1. Measurement Colocation

[10] Attempts to colocate HIRS and the GEO data are limited to within 45 degree from the GEO's nadir such that the maximum GEO zenith angle is about 60°, similar to that for HIRS. The HIRS and GEO data are considered concurrent if the relevant scanning lines were started within 15 minutes from each other. These data are then spatially colocated within the accuracy of operational navigation. A 5 × 5-pixel array of GEO measurements is used to match the HIRS field-of-view (FOV). Although the actual GEO FOV varies, this is the best overall compromise.

2.1.2. Alignment of Viewing Geometry

[11] Even if HIRS and the GEO view the same location at the same time, the measurements may differ if the location is viewed with different zenith angles. This is particularly true for the 6.7 μm channel, which is strongly affected by atmospheric attenuation. If the atmosphere is not horizontally homogeneous, even the direction of view can introduce significant differences in the atmospheric path length between HIRS and the GEO.

[12] To avoid these confusions, the difference between HIRS's and the GEO's zenith angles must be limited. Since it is the optical path within the atmosphere that must be similar between HIRS and the GEO, it was required that the difference between the secant of the two zenith

Table 1. Regression Coefficients for Deriving NOAA-14 HIRS $T_{6.7}$ and T_{11} From the Respective Geostationary Satellite[a]

Satellite	N	A	b	S_b[b]	F[c]	ρ	σ
GMS 6.7	148253	+1.93	0.9662	4.0	4.98	0.9854	0.92
GMS 11	149635	−3.98	1.0159	2.2	20.77	0.9964	0.56
G10 6.7	296765	−3.22	1.0073	1.6	40.37	0.9963	0.49
G10 11	293657	−0.12	1.0005	1.3	54.63	0.9973	0.48
G08 6.7	359351	−0.71	0.9983	1.7	33.38	0.9947	0.57
G08 11	350245	+2.60	0.9918	1.2	67.40	0.9974	0.62
M07 6.7	199892	+5.99	0.9608	3.1	9.92	0.9901	0.68
M07 11	196389	−0.58	1.0076	2.4	18.26	0.9947	0.71
M05 6.7	34381	−0.33	0.9899	8.5	1.37	0.9876	0.75
M05 11	33984	−10.59	1.0415	5.0	4.30	0.9961	0.66

[a]N is the sample size, A is the intercept of the regression, b is the slope of the regression, S_b is the standard deviation, F is the F test parameter for goodness of fit, ρ is the linear correlation coefficient, and σ is the standard deviation of the residual.
[b]Times 10^4.
[c]Times 10^6.

angles, which is proportional to the optical path, is less than 0.05. This allows rather large difference in zenith angles around the nadir (∼18°) but very small difference in zenith angles away from the nadir (∼2° when zenith angle is 45°). It was also required that, if both zenith angles are larger than 5° (i.e., neither can be regarded as nadir view) the relative azimuth angle between HIRS and the GEO must be less than 30°. These conditions ensure that the views by HIRS and the GEO are adequately aligned to minimize the difference in measurements due to viewing geometry.

2.1.3. Homogeneity of Field of View

[13] As mentioned before, an array of GEO pixels was used to match a single HIRS FOV. This match is not perfect for all GEOs. In addition, navigation errors in either system, nominally a fraction of the FOV, may further increase the magnitude of mismatch in space. To alleviate this problem, it was required that the standard deviation of the 5 × 5 GEO pixels for the 11 μm channel be less than 1 K. It is hoped that by avoiding scenes of large spatial variation, the difference in measurements due to spatial mismatch will also be reduced.

2.1.4. Intercalibration Results

[14] Recursive regression was performed for all HIRS/ GEO colocated measurements. Results are summarized in Table 1 and plotted in Figures 1 and 2. Figures 1 and 2 show that the samples are reasonably well distributed over the range of expected T_b. Therefore the statistical inference derived from these data sets should be credible. The regression slopes (b column) are generally nonunity, though some are very close to unity. Their standard deviations (S_b column) indicate that the b values are accurate to the third or higher digit after the decimal point. The columns of S_b, F, and ρ are measures of goodness of fit, and these parameters are internally consistent. The fit is generally better for GOES, worse for GMS-5, and worst for METEOSAT-5. This is consistent with the sample size. Within each satellite, the fit for the IR window channel is better than that for the water vapor channel. A better fit does not necessarily mean a better instrument unless the NOAA-14 HIRS measurements are regarded as "perfect." From a practical point of view, however, a better fit does imply better predictability of
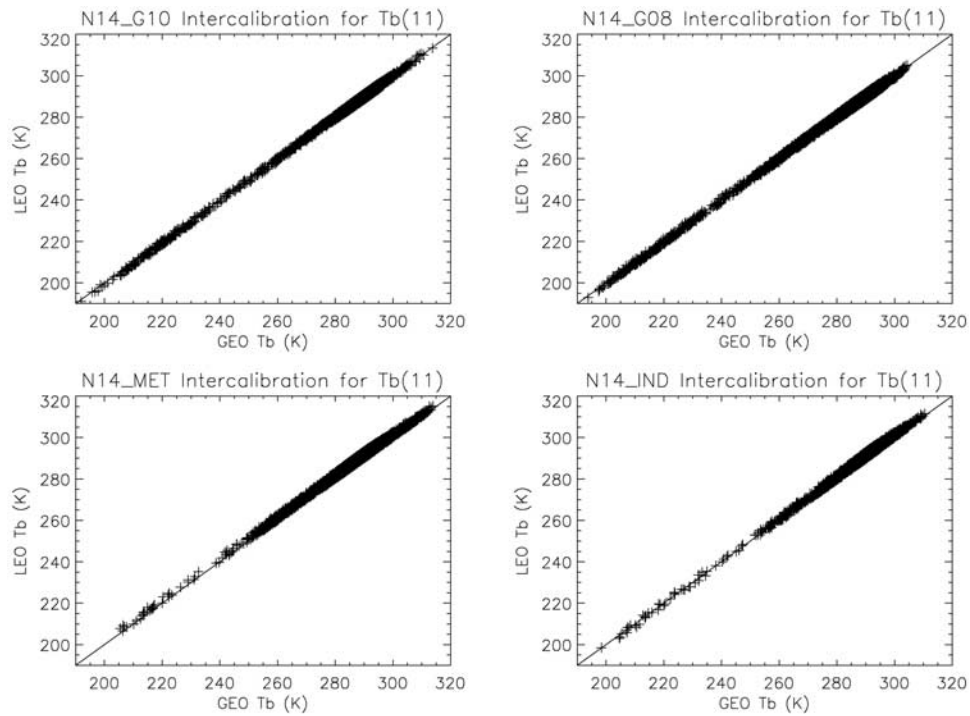
Figure 1. Scatter diagrams of the colocated NOAA-14 HIRS and GOES-10 (upper left), GOES-8 (upper right), METEOSAT-7 (lower left), and METEOSAT-5 (lower right) for the 11 μm IR window channel. Only 1/10 of randomly selected data were plotted in each diagram.

HIRS T_b using GEO T_b. The last column (σ) is a measure of how well, in an absolute sense (error in degrees K), one can estimate HIRS T_b from GEO T_b, but it is not necessarily a measure of the goodness of fit. For example,

with METEOSAT-7 the root-mean square-error (RMSE) is 0.68 K for the water vapor channel and 0.71 K for the IR window channel. Since the mean T_bs for these two channels are 246 K and 290 K, respectively, the relative
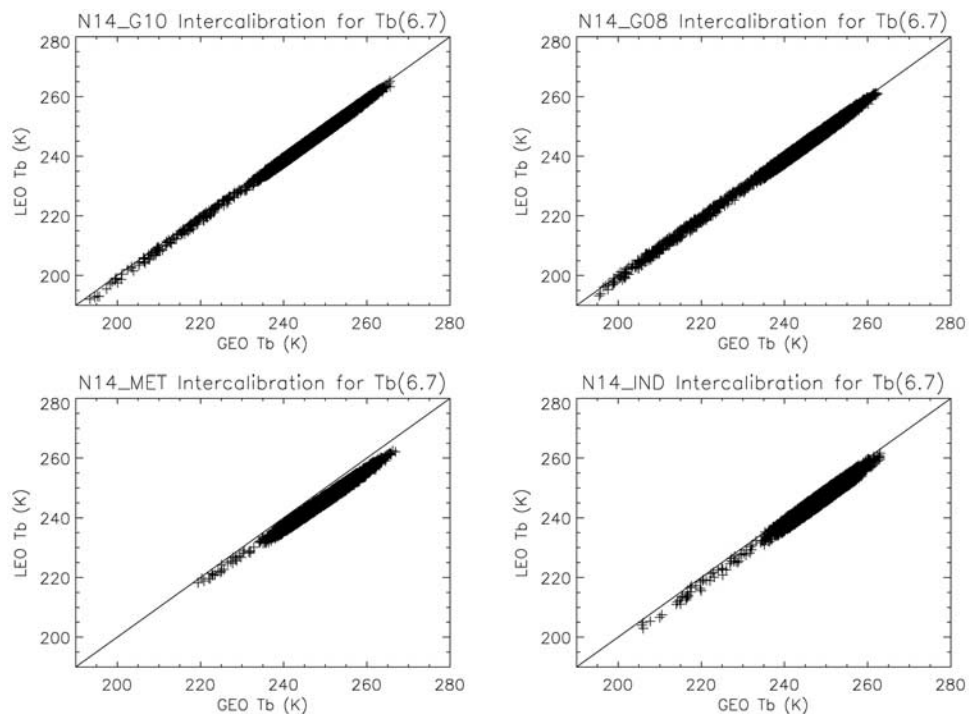

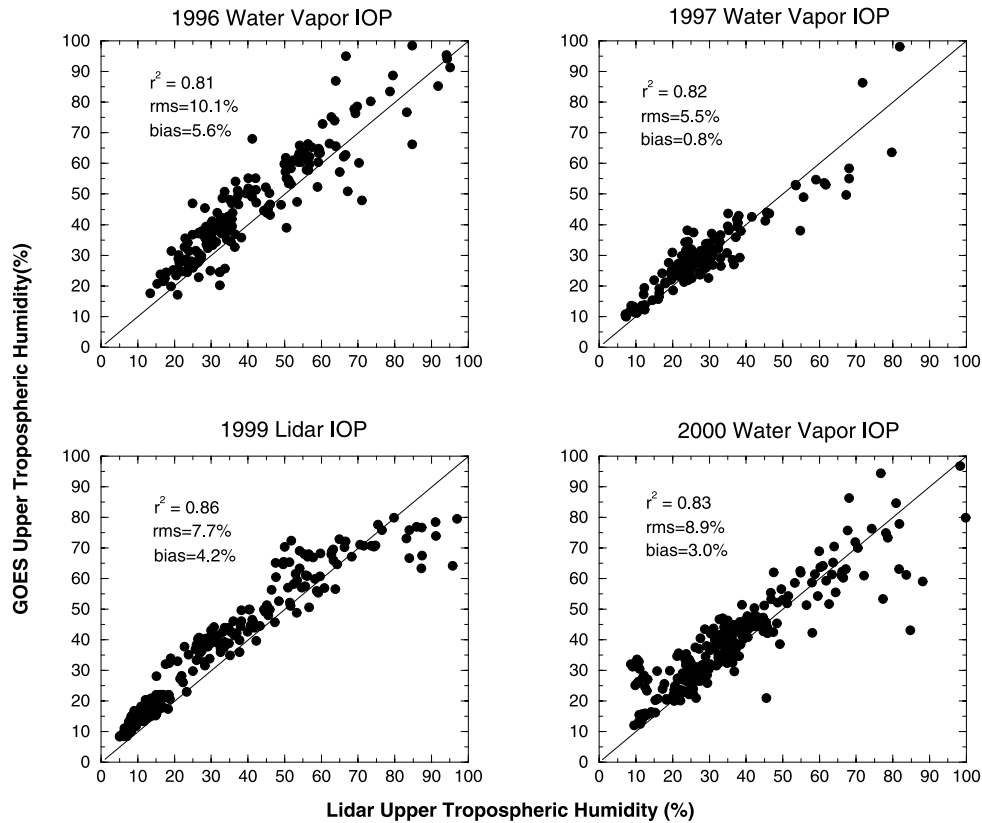**Figure 2.** As Figure 1, but for the 6.7 μm water vapor channel.

Figure 3. Verification of the satellite UTH retrieval algorithms: GOES UTH versus the colocated measurements from the CART Raman Lidar (CARL). See color version of this figure in the HTML.

error is actually smaller for the IR window channel, thus it is a better fit.

2.2. UTH, High Clouds, and Deep Convection Retrieval

[15] In this study, UTH is derived from the intercalibrated clear-sky $T_{6.7}$, following the method of *Soden and Bretherton* [1993]:

$$UTH = (\cos \theta / p_0) \exp(a + bT_{6.7}), \quad (1)$$

where, $a = 27.9$, and $b = -0.10$ are constants, θ is the satellite zenith angle, and the p_0 term account for the dependence of $T_{6.7}$ on atmospheric temperature and is calculated by $p_0 = p_{T=240}(1 + \ln(T_{6.7}/240)/\beta)$, where $p_{T=240}$ is the climatology pressure (varying with latitude, longitude and month) for atmospheric temperature at 240 K, and $\beta \equiv \partial \ln T / \partial \ln p \approx 0.23$. Interested readers please refer to *Soden and Bretherton* [1993, 1996] for further details regarding equation (1).

[16] In essence, UTH is simply an exponential stretch of the $T_{6.7}$ field that, when tuned to detailed radiative transfer calculations, provides an accurate measure of the relative humidity averaged over a broad layer in the upper troposphere (roughly 200–500 hPa). To verify the reliability of the satellite-inferred UTH, Figure 3 compares the GOES UTH to colocated measurements from the ARM CART Raman Lidar (CARL). The GOES and CARL observations exhibit excellent agreement, with systematic differences in

upper tropospheric humidity ranging from ∼5–10% [*Soden et al.*, 2004]. The high degree of consistency between the GOES and CARL observations supports the use of global geostationary observations of UTH to study the diurnal cycle in UTH and to evaluate the GCM.

[17] Since clouds strongly attenuate the upwelling radiance at 6.7 μm, estimation of UTH is only possible from high-cloud free pixels [*Soden and Bretherton*, 1993]. Thus T_{11} is also used in this study to detect high clouds and deep convection because T_{11} is mainly affected by cloud-top heights [e.g., *Fu et al.*, 1990; *Mapes and Houze*, 1993; *Hendon and Woodberry*, 1993; *Janowiak et al.*, 1994; *Chen and Houze*, 1997; *Yang and Slingo*, 2001; *Wilcox*, 2003]. We use 260 K as the temperature threshold for high clouds because the climatological temperature at 440 hPa is close to 260 K. Pixels are classified as cloudy (100% cloud cover) when $T_{11} < 260$ K. Thus we define the cloud-contaminated pixels (CLD) as follows:

$$CLD = 1, \text{ if } T_{11} < 260 \text{ K, otherwise zero.} \quad (2)$$

This temperature threshold can detect deep convective clouds (DCC, $T_{11} < 230$ K) and cirrus anvil clouds (CAC) (230 K < T_{11} < 260 K) [*Fu et al.*, 1990; *Mapes and Houze*, 1993; *Chen and Houze*, 1997], but may exclude some very thin cirrus which transmit sufficient IR radiance from below to appear warmer than 260 K. Thus the derived UTH from equation (1) using cloud-screening formula (2) may be still contaminated by some very thin cirrus. When averaged in a

grid box, although underestimated, CLD can roughly represent the high-cloud cover, especially CAC. As shown by *Fu et al.* [1990], the high-cloud amount mainly consists of CAC, while DCC occupy in a relatively small area directly associated with the deep convective core. Thus we will use CLD and CAC interchangeably through the rest of the paper.

[18] Total tropical rainfall (stratiform and convective components, collectively) for large spatial scales has been shown to be well correlated with the fractional coverage of DCC over GATE [*Arkin*, 1979]. Later *Arkin and Meisner* [1987] developed the GOES precipitation index (GPI) to derive the tropical total precipitation from the fractional coverage of DCC for the Global Precipitation Climatology Project (GPCP) [*Xie and Arkin*, 1997]. Instead of using the fractional coverage of DCC, *Hendon and Woodberry* [1993] used the actual temperature difference between 230 K and $T_{11} < 230$ K to infer the tropical deep convection and total precipitation (referred to as precipitation index (PI) in this study, mm day^{-1}):

$$PI = a(230 - T_{11}), \text{ if } T_{11} < 230 \text{ K, otherwise zero.} \quad (3)$$

Here $a = 6.96$ mm day^{-1} K^{-1}. This PI gives more weight to colder clouds because the actual difference in temperature is used. As shown by *Fu et al.* [1990], the coldest clouds have the highest albedos and hence are associated with deep convection. Thus this PI is biased toward the cold-bright regime. *Yang and Slingo* [2001] shows that the seasonal mean precipitation produced by (3) from the CLAUS data compares well with other precipitation climatology [e.g., *Xie and Arkin*, 1997]. In this study, we use formula (3) to infer the tropical precipitation associated with deep convection and DCC from satellite observations.

[19] Theoretically, we need to convert T_{11} to an equivalent nadir T_{11} to eliminate the viewing angle dependence before equations (2) and (3) can be applied. The radiative transfer calculations indicate that the difference between the nadir T_{11} and the actual T_{11} is small, generally less than 0.5 K in most regions, except at the satellites boundaries, which are around $1-2$ K. This small difference should not significantly affect the PI and CLD derived from equations (2) and (3). Thus we did not attempt the zenith angle correction for T_{11}.

[20] For comparisons to AM2/LM2, we have spatially averaged the radiances and the derived variables into the GCM grid ($2.5° \times 2.0°$ longitude-latitude) with a minimum of 50 pixels (10%) of good data in a grid box. Sensitivity studies indicate that the mean UTH and its diurnal cycle of UTH are not very sensitive to this threshold. If we increase this threshold, UTH will be biased toward to dry regions (UTH decreases slightly, around 5%), and there will be large data voids in the diurnal cycle map, and vice versa.

2.3. GFDL AM2/LM2 Simulations

[21] For the AM2/LM2 evaluation, we have integrated the frozen version AM2p12b of the new GFDL coupled atmosphere and land model, known as AM2/LM2 (Anderson et al., submitted manuscript, 2004), for 17 years from the cold start (1 January 1982) with the prescribed daily Reynolds optimum interpolation sea surface temperature (SST) interpolated from its monthly mean [*Reynolds*

et al., 2002]. However, there is no diurnal cycle in the prescribed SST and its possible effects on the model diurnal cycle of convection, clouds, and water vapor will be discussed later. The atmosphere model, known as AM2, includes a new grid point dynamical core, a prognostic cloud scheme, and a multispecies aerosol climatology, as well as components from previous models used at GFDL. The latitude-longitude horizontal grid is a staggered Arakawa B grid with resolution 2.5° longitude by 2.0° latitude. In the vertical, a 24-level hybrid coordinate grid is used with the effective model top at about 40 km. The cloud scheme consists of the prognostic microphysics (cloud liquid and ice) parameterization of *Rotstayn* [1997] and the prognostic macrophysics (cloud fraction) parameterization from *Tiedtke* [1993]. Moist convection is represented by the Relaxed Arakawa-Schubert (RAS) formulation of *Moorthi and Suarez* [1992] with the detrainment of cloud liquid, ice, and fraction from convective updrafts into stratiform clouds. The full configuration of the GFDL AM2/LM2 and its climatological performance can be found in the work of Anderson et al. (submitted manuscript, 2004).

[22] The 3-hourly instantaneous output of temperature, specific humidity, cloud amount, liquid and ice water contents, and total precipitation (3-hour accumulation) have been archived for 1999. Adopting the "model-to-satellite approach" [*Morcrette*, 1991], we use the temperature, humidity, cloud amount, and liquid and ice water profiles from AM2/LM2, and a generalized forward radiative transfer model for HIRS-14 [*Soden et al.*, 2000] to simulate the clear-sky and total-sky $T_{6.7}$ and T_{11}, which can be easily compared with the satellite observed $T_{6.7}$ and T_{11}. In the calculations of the total-sky $T_{6.7}$ and T_{11}, the random overlap assumption is applied for clouds. The model high-cloud amount is diagnosed from the model cloud amount above 440 hPa under the random overlap assumption used by AM2. The model UTH is derived from the model-simulated clear-sky $T_{6.7}$ for model grids where high-cloud amount is less than 90% using formula (1), consistent with satellites. Thus, for both satellites and AM2/LM2, the following five physical quantities with spatial resolution 2.5° longitude by 2.0° latitude and temporal resolution 3 hours will be used in this study to examine the satellite-observed and model-simulated diurnal cycle of deep convection, precipitation, high clouds and upper tropospheric water vapor: T_{11}, $T_{6.7}$, UTH, CLD (high_cld_amt) and PI (precip).

2.4. Data Analysis

[23] Two diurnal cycle analysis methods, time series analysis and histogram analysis, have been used in this study following *Soden* [2000] and *Yang and Slingo* [2001]. For each physical quantity at each grid box, a "composite day" was first constructed by averaging these fields at 3-hour intervals from each day of each month. A minimum of 15 days with quality data is required for the average; otherwise it is considered missing. For each composite day, if there is only one 3-hour time step with missing data, then this missing value is replaced by the linear interpolation from adjacent 3-hour time steps. Otherwise, the composite day was disregarded. The resulting composite day was then decomposed spectrally using a Fourier transform to obtain the amplitude (hereafter, "diurnal amplitude") and phase

(hereafter, "diurnal phase") of the first diurnal (24 hour) harmonic. The diurnal phase corresponds to the local time of the considered variable's maximum. For example, for each variable P, we have

$$P(t) = P_0 + A \cos\left[\frac{2\pi}{24}(t - \sigma)\right] + \text{residual} = P_0 + a \cos\left(\frac{2\pi}{24}t\right)$$
$$+ b \sin\left(\frac{2\pi}{24}t\right) + \text{residual,} \quad (4)$$

where P_0 is the daily mean, and $A = \sqrt{a^2 + b^2}$ is the diurnal amplitude (note: the peak-to-peak amplitude is 2A). σ is the diurnal phase and t is LST, both expressed in hours. To quantify the relative importance of the diurnal cycle, the relative diurnal amplitude is also computed by normalizing the diurnal amplitude by the daily mean, that is, $A_r = A/P_0 \times 100\%$. The diurnal amplitude and phase will be displayed in a vectorial format (Figures 4 and 5) in a map to highlight the spatial consistency of the diurnal cycle and land-sea contrast [e.g., *Wallace*, 1975].

[24] The histograms of T_b have also been used extensively for the diurnal cycle studies [e.g., *Albright et al.*, 1985; *Hartmann and Recker*, 1986; *Chen and Houze*, 1997; *Soden*, 2000; *Yang and Slingo*, 2001]. In this study, the observed $T_{6.7}$, T_{11}, and UTH at each grid were first binned into 5-K (5%) intervals for each 3-hour period and each month. Then the percentage of grids within each bin was calculated by dividing the number of grids at each bin by the total number of grids for each 3-hour period and each month. Finally, the diurnal anomalies of the percentage histogram are constructed by removing its daily mean separately for each bin to highlight the diurnal cycle (Figures 6 and 7). This histogram analysis has been applied over both land and ocean regions over the whole tropics to highlight the land-sea contrast. We have analyzed the diurnal cycles from satellites and AM2/LM2 for four months of 1999, January, April, July and October, and a similar diurnal cycle is found for four seasons. Thus we will mainly present the results from July 1999.

3. Observed Diurnal Cycle From Satellites
3.1. Diurnal Amplitude and Phase

[25] Figure 4 shows the diurnal amplitudes and phases of deep convection/precipitation (PI, row 1), high-cloud amount (CLD, row 2), total-sky T_{11} (row 3), and UTH (row 4). The length of the arrow depicts the diurnal amplitude (see key on inset). The diurnal phase can be determined from the orientation of the arrows with respect to a 24-hour clock. Arrows pointing upward indicate a peak at 0000 LST (midnight), downward indicate a peak at 1200 LST (noon), toward the right indicate a peak at 0600 LST (dawn), and toward the left a peak at 1800 LST (sunset). For better visual results, we have spatially smoothed the diurnal amplitude and phase at the expense of clear land-sea contrast at coastal regions for some variables, such as T_{11}.

[26] Large diurnal variations in deep convection and precipitation (around $2-10$ mm day^{-1}) are observed over the deep convective regions, such as equatorial Africa, Central and North America, and the "Marine Continent" of the western Pacific and southeastern Asia as well as the intertropical convergence zone (ITCZ) and southern Pacific

convergence zone (SPCZ) [e.g., *Hendon and Woodberry*, 1993; *Soden*, 2000; *Yang and Slingo*, 2001]. In general, the more intense the deep convection, the stronger its diurnal variation [*Gray and Jacobson*, 1977]. This is true over both land and ocean. Figure 4 shows a clear land-sea contrast in the diurnal cycle of deep convection and precipitation. Over land, the diurnal variation of deep convection and precipitation is stronger (around $4-10$ mm day^{-1}) and comparable to its daily mean, and maximum deep convection and precipitation occurs in the late afternoon and early evening (1700–2200 LST). On the other hand, the diurnal variation of deep convection and precipitation is relatively weaker (around $1-3$ mm day^{-1}) over ocean, and only about 20% of its daily mean. The oceanic deep convection and precipitation tends to peak around early morning (0600–1000 LST). Moreover, some regional variations in the diurnal cycle in deep convection are also evident, such as the Bay of Bengal and the northwestern Pacific. The deep convection tends to peak around noon and early afternoon, between the diurnal phases of deep convection over ocean and land. This indicates that the diurnal variation of deep convection over the coastal ocean may be triggered by the diurnal cycle of deep convection over the nearby land [*Yang and Slingo*, 2001]. The present results of the diurnal variations of deep convection and precipitation generally agree with previous studies based on surface observations [e.g., *Wallace*, 1975; *Gray and Jacobson*, 1977; *Dai*, 2001], satellite IR radiances [e.g., *Hendon and Woodberry*, 1993; *Janowiak et al.*, 1994; *Chen and Houze*, 1997; *Soden*, 2000; *Yang and Slingo*, 2001], passive microwave radiometers [e.g., *Chang et al.*, 1995; *Imaoka and Spencer*, 2000], and precipitation radar [e.g., *Nesbitt and Zipser*, 2003].

[27] Large diurnal variations (around 10%) in high-cloud amount (mainly CAC) are also observed over the deep convective regions where high clouds are persistent [e.g., *Udelhofen and Hartmann*, 1995; *Bergman and Salby*, 1996; *Soden*, 2000]. Similar to deep convection, there exists a clear land-sea contrast in the diurnal cycle of high clouds. The diurnal variation of high clouds is stronger (around 10% and about half of its daily mean) over land, and typically peaks in the late evening (2000–2400 LST). However, it is relatively small (around 4% and about 10% of its daily mean) over ocean, and typically peaks in the late afternoon (1500–1800 LST) [e.g., *Udelhofen and Hartmann*, 1995; *Bergman and Salby*, 1996; *Soden*, 2000]. As shown later, this land-sea contrast in the diurnal cycle of deep convection and high clouds is also well captured and can be explained by the histogram of T_{11} (Figure 6) [*Soden*, 2000].

[28] Significant diurnal variation of T_{11} is observed over the tropics, and its spatial variations can be explained by the spatial variation of the diurnal cycle in high clouds (mainly CAC) and surface temperature. The largest diurnal amplitude of T_{11}, around 10 K, occurs over clear-sky land regions (high-cloud free), such as Saudi Arabia and the Sahara desert, as a result of the large response of the land surface temperature to daytime solar heating [*Hendon and Woodberry*, 1993; *Yang and Slingo*, 2001]. They tend to maximize about $1-2$ h after the peak in solar heating, indicating a slight lag in land surface heating due to the thermal inertia of the soil. Other regions of significant diurnal variations in T_{11} are deep convective regions, with
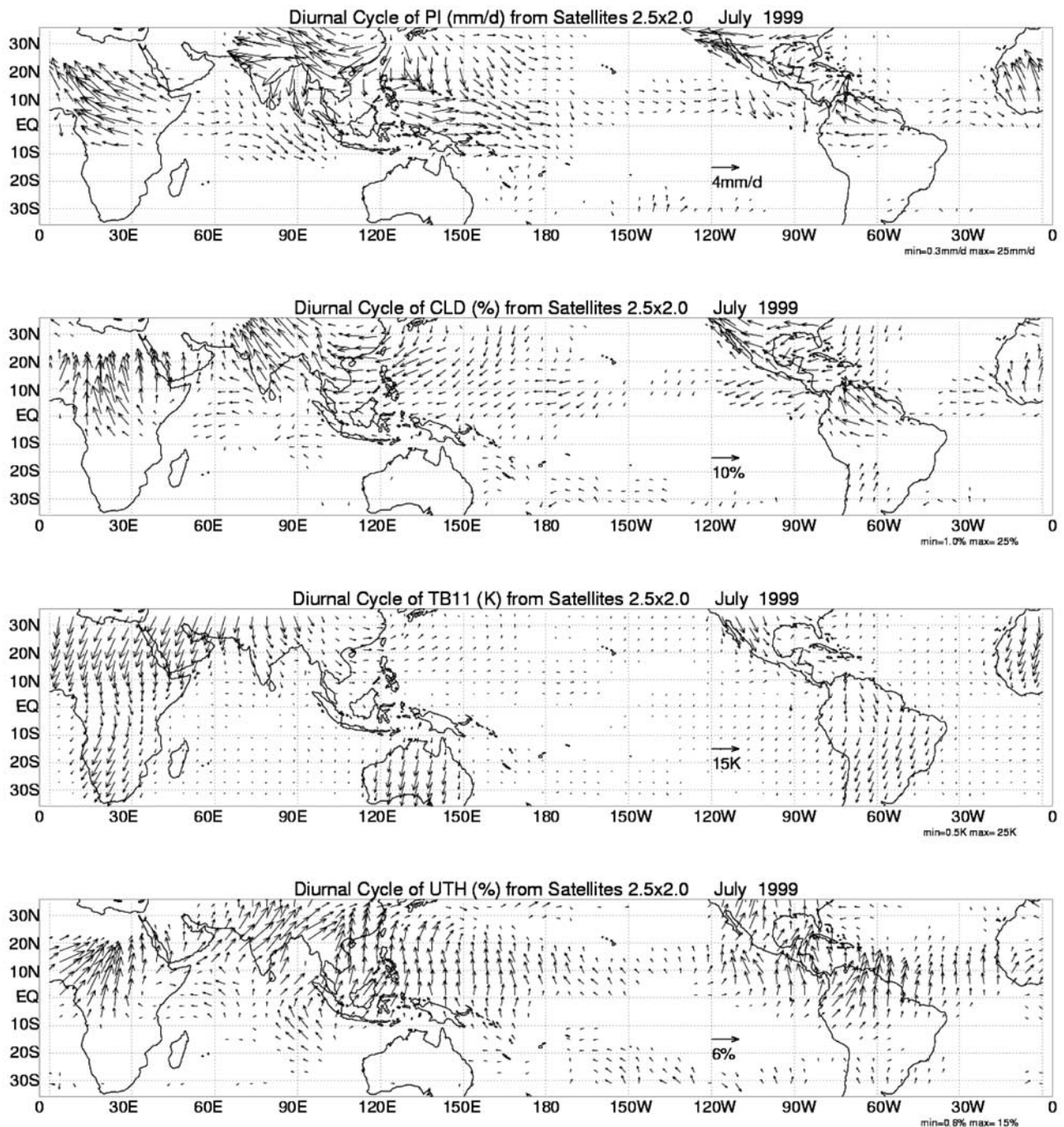
Figure 4. Satellite-observed diurnal amplitudes and phases of deep convection/precipitation (PI, row 1), high-cloud amount (CLD, row 2), T_{11} (row 3), and UTH (row 4), monthly averaged for July 1999. The units are mm day^{-1} for PI, % for CLD and UTH, and K for T_{11}. The length of the arrow depicts the diurnal amplitude (see key on inset). The diurnal phase corresponds to the local time of maximum and can be determined from the orientation of the arrows with respect to a 24-hour clock. Arrows pointing upward indicate a peak at 0000 local standard time (LST) (midnight), downward indicate a peak at 1200 LST (noon), toward the right indicate a peak at 0600 LST (dawn), and toward the left a peak at 1800 LST (sunset). For clarity, results are only shown where the amplitude is above the specified value (see min at the right bottom of the figure).

a clear distinction between land and ocean. Over the deep convective land regions, such as equatorial Africa, southeastern Asia, and Central and North America, the diurnal amplitude of T_{11} is around 8 K, and tends to peak around late morning (1000–1100 LST). This may be a combined result of the diurnal cycle of land surface temperature (peaking 1–2 hours after noon) and upper level clouds that experience a diurnal minimum in the late morning. Over
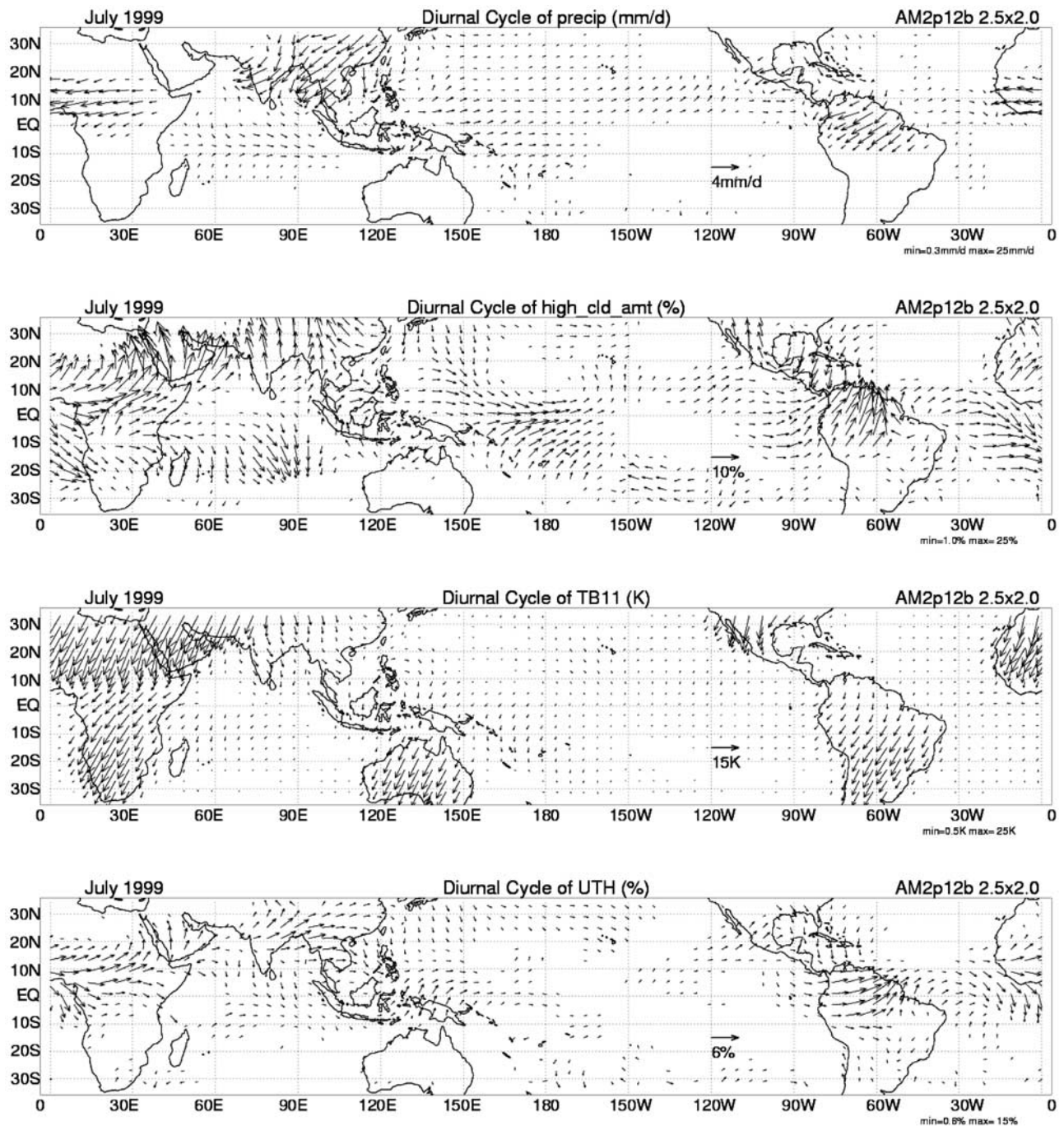
Figure 5. The diurnal amplitudes and phases in AM2/LM2 precipitation (row 1), high-cloud amount (row 2), total-sky T_{11} (row 3), and UTH (row 4), monthly averaged for July 1999. Others are same as in Figure 4.

the oceanic deep convective regions, the diurnal amplitude of T_{11} is around 1 K, and tends to peak in the early morning (0400–0800 LST) when oceanic high clouds experience a diurnal minimum. Over the low cloud regimes off the west coast of South America, the diurnal amplitude of T_{11} is also noticable, around 1 K. They tend to peak in the midafternoon (1500 LST) when low clouds experience a diurnal minimum [e.g., *Rozendaal et al.*, 1995; *Bergman and Salby*, 1996]. The diurnal cycle of T_{11} over the oceans may be mainly regulated by the diurnal cycle of oceanic clouds due to the small diurnal amplitude of SST [*Webster et al.*, 1996; *Chen and Houze*, 1997; *Stuart-Menteth et al.*, 2003]. These results of the diurnal cycle of T_{11} are consistent with the CLAUS data presented by *Yang and Slingo* [2001], the global cloud imagery data presented by *Hendon and Woodberry* [1993], and the diurnal cycle of OLR by *Hartmann and Recker* [1986].
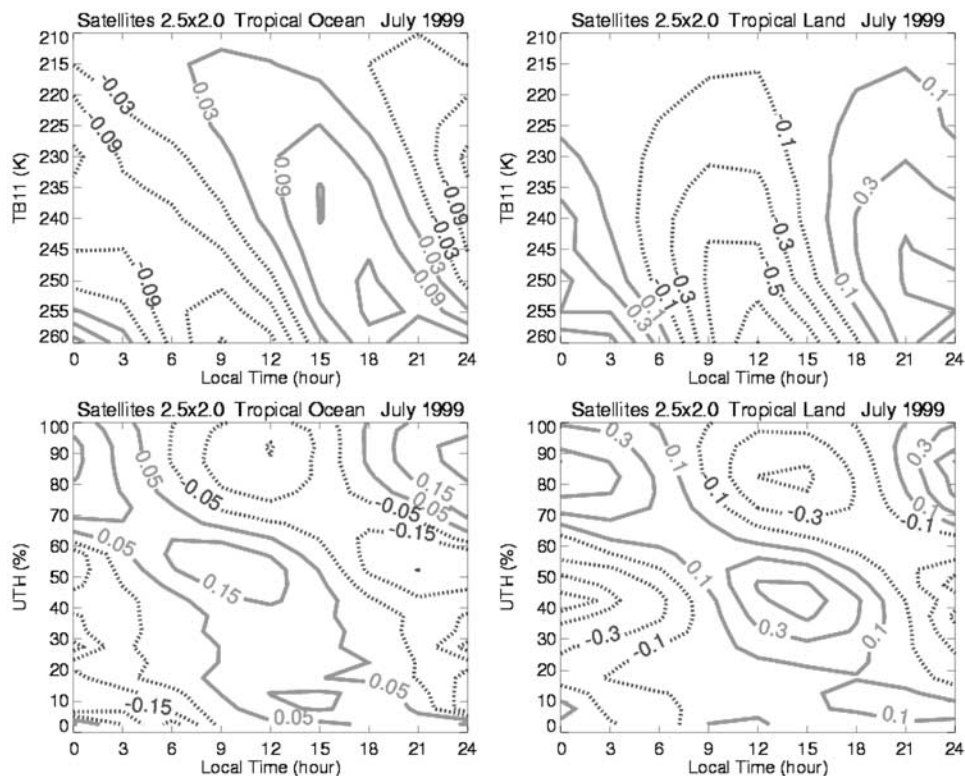
Figure 6. A histogram of the percentage of grids for which satellite-observed T_{11} (row 1), and UTH (row 2) occurred within each 5 K (5%) interval for July 1999. The left column is for tropical ocean regions and the right for the tropical land regions. See color version of this figure in the HTML.

[29] Interestingly, similar to deep convection and high clouds, large coherent diurnal variations (around 6%) in UTH are also observed over the deep convective regions where the daily mean UTH is high. In other words, the moister the upper troposphere, the stronger the diurnal cycle of UTH. Furthermore, similar to deep convection and high clouds, the land-sea contrast in the diurnal cycle of UTH is also clear but relatively smaller. The diurnal variation of UTH is relatively stronger (around 4–6% and about 10% of its daily mean) over land, whereas it is relatively weaker (around 2–4% and about 6% of its daily mean) over ocean. UTH generally peaks around early morning (0300 LST) over land in contrast to midnight (0000 LST) over the oceans. In other words, the diurnal phase of UTH over land is about 3 hours later than that over ocean. The current diurnal phase in UTH differs from *Udelhofen and Hartmann* [1995] by about 6 hours, but is consistent with *Soden* [2000] based on satellite-observed $T_{6.7}$ and *Dai et al.* [2002] based on radiosonde data.

3.2. Diurnal Anomalies

[30] Clearly, there exists a distinct lag in the phase-relationships between UTH, high-cloud amount, and deep convection as shown in Figure 4. To better understand the diurnal cycle relationship between UTH, high clouds, and deep convection, the monthly mean diurnal anomalies of the tropical mean deep convection/precipitation, high-cloud amount, and UTH are shown in Figure 8. Tropical mean refers to the spatial-weighted average from 30°S to 30°N, calculated separately for ocean (left) and land (right) regions to highlight the land-sea contrast. Consistent with studies by

Soden [2000], Figure 8 shows that UTH (peaking around midnight over ocean and around 0300 LST over land) lags high clouds (peaking around 1600 LST over ocean and around 2100 LST over land) by about 6–8 hours, and high clouds further lag deep convection by about 3–9 hours. This phase lag relationship between UTH, high clouds, and deep convection indicates that the diurnal cycle of UTH is regulated by the diurnal cycle of deep convection and high clouds. This is also consistent with the traditional view that deep convection serves to moisten the upper troposphere [e.g., *Betts*, 1990; *Sun and Lindzen*, 1993; *Soden and Fu*, 1995; *Soden*, 1998, 2000; *Held and Soden*, 2000]. In particular, the above phase lags indicate that UTH is more directly influenced by CAC generated by the deep convection instead of DCC within the deep convective core [*Betts*, 1990; *Soden*, 2000]. To further demonstrate this point, we have plotted the joint probability distribution function (JPDF) of T_{11} and UTH over the tropical oceans (similar results for land) (Figure 9). It is very clear that high UTH (>70%) are mostly associated with CAC whose tops are between 230 K and 260 K instead of the very cold DCC (T_{11} < 230 K). As pointed out by *Betts* [1990], tropical convective systems usually start with DCC within a very small deep convective core, but then they develop into mesoscale anvil ice clouds through the detrainment of ice and liquid from DCC. The decay of these thick upper level anvil clouds leaves large amounts of water in the upper troposphere, which is the major source of UTH [*Soden*, 2000]. This demonstrates that understanding the life cycle of mesoscale CAC is very important to understanding water vapor feedback and global warming [*Betts*, 1990].
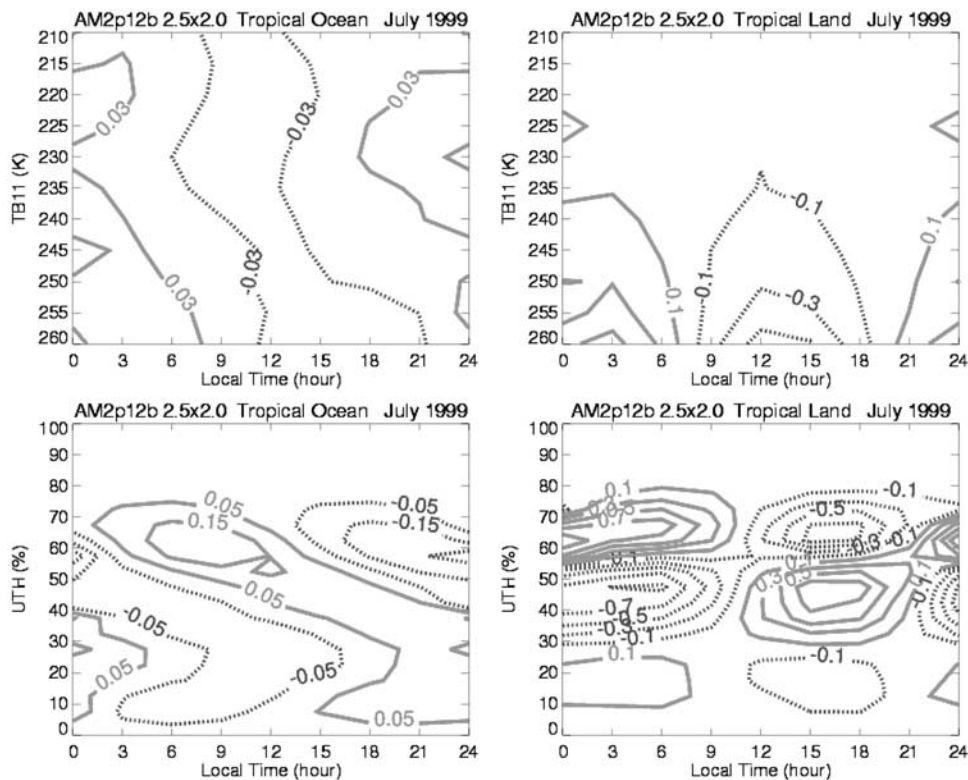
Figure 7. Same as Figure 6 except for AM2/LM2. See color version of this figure in the HTML.

[31] Figure 8 clearly shows the strong land-sea contrast in diurnal amplitudes, which are bigger over land and smaller over ocean. When spatially averaged over the whole tropics, the diurnal amplitudes of PI, CLD, and UTH over ocean are about 0.48 mm day^{-1}, 1%, and 1%, or about 18%, 9%, and 3% of their daily means, respectively. On the other hand, the diurnal amplitudes of PI, CLD, and UTH over land are around 1.87 mm day^{-1}, 4%, and 2.2%, or about 55%, 28%, and 6% of their daily means, respectively. It is interesting to note that the diurnal magnitude of PI over ocean is very close to the results of *Imaoka and Spencer* [2000] and *Chang et al.* [1995] based on passive microwave radiometers.

3.3. Histograms of T_{11} and UTH

[32] Figure 8 also shows that there is a clear land-sea contrast in the diurnal phase relationship between UTH,

high clouds, and deep convection. The phase lag between high clouds and deep convection is longer over the oceans than land. To better understand this land-sea contrast, Figure 6 shows the histograms of the percentage of grids for which total-sky T_{11} (row 1) and UTH (row 2) occurred within each 5 K (5%) interval with its daily mean removed separately for each bin. The left column is for tropical ocean regions, and the right for the tropical land regions. It is worthwhile to mention that the histogram of T_{11} based on averaged T_{11} over $2.5° \times 2.0°$ longitude-latitude grids is very similar to that based on T_{11} over $0.1° \times 0.1°$ longitude-latitude pixels, consistent with the findings by *Hartmann and Recker* [1986]. Clearly, there exists a strong land-sea contrast in the tropical convective clouds. The histogram in T_{11} over land (Figure 6, top right) reveals a coherent vertical structure with peak high cloudiness occurring in the early
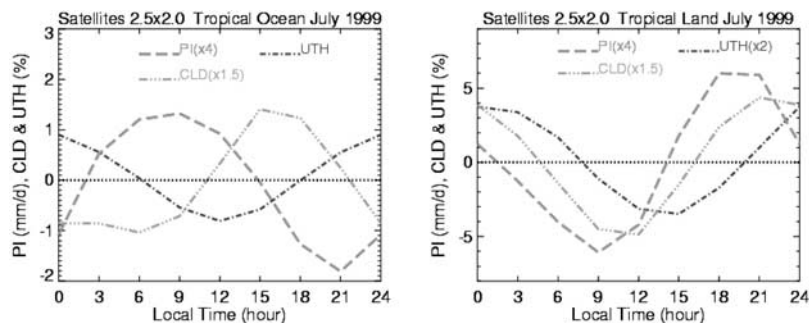

Figure 8. The satellite-observed diurnal anomalies in deep convection/precipitation (PI, mm/d), high-cloud amount (CLD), and UTH (%) for spatial-weighted average over tropical ocean (left) and tropical land (right) regions. See color version of this figure in the HTML.
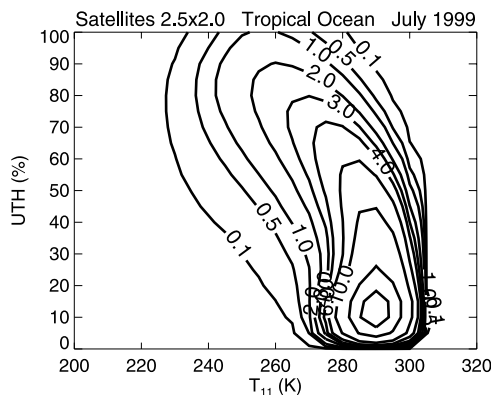
Figure 9. The joint probability distribution function of T_{11} and UTH from satellites over the tropical oceans.

evening (2100 LST), for a broad range of cloud-top heights (210 K < T_{11} < 250 K, about 150–400 hPa) [*Soden*, 2000; *Yang and Slingo*, 2001]. Thus the phase lag between high clouds and deep convection is small. Both DCC and CAC develop in the afternoon, reach maximum in the evening, and then decay and dissipate during the early morning [*Yang and Slingo*, 2001]. Over land, the diurnal cycle of the convective cloud systems can be mainly attributed to a direct thermodynamic response to the strong diurnal cycle of the land surface temperature [*Wallace*, 1975]. During the day, the solar heating increases the land surface and lower-tropospheric temperature, and thus atmospheric instability, leading to the rapid development of convective cloud systems, for a broad range of cloud-tops (210 K < T_{11} < 250 K). These convective clouds soon reach maximum in the evening. At night, strong radiative cooling decreases the land surface and lower-tropospheric temperature, and thus enhances atmospheric stability, and suppresses convection. The convective cloud systems then decay and dissipate quickly during the early morning [*Yang and Slingo*, 2001].

[33] The oceanic convective clouds, on the other hand, exhibit a distinct vertical phase lag. For example, DCC peak in the early morning (0600 LST). However, at roughly the same time, CAC experience a diurnal minimum, and then peak in the late afternoon (1500–1800 LST) [*Soden*, 2000]. This is consistent with the large phase lag, about 8 hours, between oceanic high-cloud amount (CLD) and deep convection/precipitation (PI) (Figure 8). This downward phase

propagation from early morning maximum for DCC to late afternoon maximum for CAC has been extensively documented by previous studies, such as *Albright et al.* [1985], *Hartmann and Recker* [1986], *Mapes and Houze* [1993], *Chen and Houze* [1997], *Soden* [2000], and *Yang and Slingo* [2001]. However, the physical mechanisms behind the diurnal cycle of oceanic convective clouds remain poorly understood, and are still a subject of intense research. One mechanism, first proposed by *Gray and Jacobson* [1977], emphasizes the dynamical consequence of the daily variations of the convective-clear differential radiative heating producing a daily variation in the horizontal divergence field, modulating the convection. A second mechanism involves a direct radiation-convection interaction [e.g., *Randall et al.*, 1991]. At night, IR cooling at cloud tops results in the destabilization of the upper troposphere, leading to the convection development with a maximum occurring in the early morning. In contrast, during the day, warming at cloud tops due to solar absorption by clouds and water vapor increases the static stability, and therefore depresses convective activities. Recently, *Chen and Houze* [1997] ascribed the diurnal cycle of oceanic convection to a combined result of the diurnally varying SST and the life cycle of convective cloud systems, especially the spatially large systems. SST has a weak but noticeable diurnal cycle (∼0.5–1 K), especially in low wind speed regions such as the ITCZ and SPCZ, and generally peaks in the early afternoon [e.g., *Webster et al.*, 1996; *Chen and Houze*, 1997; *Stuart-Menteth et al.*, 2003]. The spatially large convective systems have a strong tendency to form in the afternoon, when the surface conditions are most favorable, that is, higher SST. These systems usually undergo a life cycle of about one day; they reach their maximum area extent of very cold cloud tops during night-to-dawn hours, and subsequently decay after sunrise. During the daylight hours of the following day, as part of the cloud-system life cycle, the cloud tops continue to expand, but become warmer as a result of solar absorption and/or collapsing. Consequently, the area of DCC diminishes after sunrise, while the area of CAC increases. It is possible that these physical mechanisms act together to modulate the diurnal cycle of oceanic convective clouds.

[34] Similarly, the histograms of UTH also show a clear land-sea contrast. For example, for all UTH (0–100%), the diurnal amplitude is always stronger over land than ocean and the diurnal phase is always about 3 hours later over land
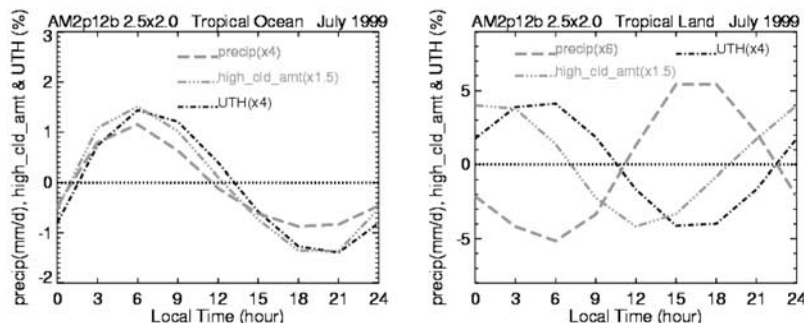

Figure 10. The diurnal anomalies in precipitation (mm/d), high-cloud amount, and UTH (%) for spatial-weighted average over tropical ocean (left) and tropical land (right) regions for AM2/LM2. See color version of this figure in the HTML.
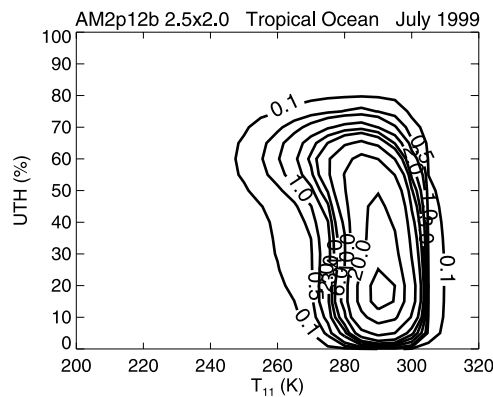
Figure 11. The joint probability distribution function of T_{11} and UTH from AM2/LM2 over the tropical oceans.

than ocean. In addition, there is also a strong phase contrast between high (>65%) and low (<65%) UTH. The high UTH, usually associated with deep convection and upward motions, generally peaks around midnight over ocean in contrast to 0300 LST over land. In contrast, at the same time, the low UTH, usually associated with the downward motions, experiences a diurnal minimum. Near noon, when the high UTH reaches its diurnal minimum, the low UTH reaches its diurnal maximum. Consequently, low clear-sky $T_{6.7}$ (resulting from high UTH) generally peaks around midnight with a diurnal minimum around noon. In contrast, high clear-sky $T_{6.7}$ (resulting from low UTH) generally peaks around noon with a diurnal minimum around midnight (figures not shown). It is interesting to note that the diurnal phase of high UTH is consistent with the diurnal phases of UTH over the tropical deep convective regions shown in Figure 4 and the tropical mean phases shown in Figure 8. This consistency and the strong phase contrast between high and low UTH indicate that the diurnal cycle of UTH is mainly contributed by the diurnal cycle of high UTH.

4. Simulated Diurnal Cycle in the GFDL AM2/LM2

[35] Figure 5 shows the diurnal amplitudes and phases of precipitation (row 1), high-cloud amount (row 2), total-sky T_{11} (row 3), and UTH (row 4) from the AM2/LM2. The diurnal anomalies in precipitation (mm/d), high-cloud amount, and UTH (%) for spatial-weighted average over tropical ocean (left) and tropical land (right) regions from AM2/LM2 are shown in Figure 10. Meanwhile, Figure 11 shows the JPDF of total-sky T_{11} and UTH from AM2/LM2 similar to Figure 9. Furthermore, Figure 7 shows the histograms of total-sky T_{11} and UTH from AM2/LM2 similar to Figure 6. As shown in Figure 5, the basic spatial variation in the diurnal cycle of precipitation, high-cloud amount, and UTH is roughly captured by AM2/LM2, that is, the strong diurnal cycle in precipitation, high-cloud amount, and UTH is mostly found in the model's deep convective regions. However, there are some clear deficiencies in the spatial pattern of the diurnal cycle, which may be associated with the deficiency of the model's mean state in precipitation, high-cloud amount, and UTH (Anderson et al., submitted

manuscript, 2004). In general, the model's mean UTH is underestimated over the moist convective regions, while it is overestimated in the dry regions. The model's mean precipitation is underestimated over the deep convective regions, and has a double ITCZ tendency. The model's mean high-cloud amount is much higher than CLD, probably due to the underestimation of thin cirrus by formula (2) and/or overestimation of high cloud amount in the model, which needs further investigation in the future.

4.1. AM2/LM2 Diurnal Cycle Over Land

[36] First, we discuss the model-simulated diurnal cycle features of precipitation, high-cloud amount, and UTH over land. The model's precipitation tends to peak around late afternoon (1500–1800 LST), and have a minimum near dawn (0600 LST), about 3 hours earlier than observations. This result is similar to the result of *Betts and Jakob* [2002], who found that the maximum of ECMWF precipitation over the Amazonia is several hours earlier than observed. For both high-cloud amount and UTH, the simulated diurnal phases are about 3 hours later than observed. Given the uncertainty of the observed diurnal phase resulting from the 3-hour resolution, we can see that AM2/LM2 can roughly capture the diurnal phases of precipitation, high clouds, and UTH over land. However, the diurnal magnitudes of precipitation, high-cloud amount, and UTH are noticeably weaker in the model compared to satellites. The simulated diurnal amplitudes of precipitation and UTH are about two thirds of the observed values, as are their relative magnitudes. The simulated relative diurnal amplitude of high clouds is only about 50% of the observed value although the actual diurnal amplitude is comparable to its observed counterpart. This is probably due to the higher mean high-cloud amount in the model as discussed above.

[37] The same diurnal phase of high cloudiness for a broad range of cloud-top heights (210 K < T_{11} < 250 K) is reasonably well simulated by AM2/LM2 except for a later peak. The vertical phase structure of UTH is also roughly captured by AM2/LM2, with high UTH (>55%) peaking in the early morning and low UTH (<55%) peaking in the afternoon. However, the observed strong diurnal variations of very high UTH (>80%) are totally missing in AM2/LM2. This may contribute to the small diurnal amplitude of UTH in the model. This deficiency also exists over the oceans and will be mentioned later. As discussed earlier, the daily mean UTH is underestimated over the deep convective regions in the model, which is also demonstrated in Figure 11. For example, very high UTH (>80%) is seldom found in AM2/LM2 in stark contrast to the high frequency of very high UTH in observations (Figure 9). The underestimation of the daily mean UTH is probably the main contributor to the lack of the diurnal cycle of very high UTH in AM2/LM2. Satellites also show that UTH increases almost linearly with the intensifying convection when UTH is above 50% (Figure 9). However, in the model, when UTH is above 50%, UTH seems to be decoupled from convection. This indicates that the moistening of the upper troposphere by the evaporation of CAC may not be well handled by the model's convection parameterization.

[38] Over clear-sky land regions (no high clouds), the simulated diurnal phase and magnitude of T_{11} (surface temperature) are both comparable to the satellite results

and may be even stronger in the model. This suggests that the daytime solar heating and nighttime radiative cooling near the land surface is well represented in AM2/LM2. Despite this, the simulated diurnal amplitudes of precipitation, deep convection, high-cloud amount, and UTH over land are still too weak, compared to satellites. This indicates that there may exist obvious deficiencies in the model's convection and cloud parameterization schemes.

4.2. AM2/LM2 Diurnal Cycle Over the Oceans

[39] Over the oceans, the model's precipitation peaks around early morning (0600 LST), consistent with satellites. However, the simulated diurnal magnitude of precipitation is only about 50% of the observed diurnal amplitude of PI, especially in the oceanic deep convective regions. The tropical mean relative diurnal magnitude of precipitation over ocean is about 8%, also about half of the observed value.

[40] Compared to satellites, AM2/LM2 also significantly underestimates the relative diurnal magnitude of oceanic high clouds, which is only about 50% of the observed value. Furthermore, the model-simulated oceanic high clouds are nearly 12 hours out of phase with observations, for a broad range of high cloud-tops (210 K < T_{11} < 260 K) including both DCC and CAC. For example, the simulated oceanic DCC peak in the late evening (2300 LST) (Figure 7) in stark contrast to the observed maximum at early morning (Figure 6). This is also true for CAC that peak in the early morning (0600 LST) in the model (Figures 5, 7, and 10) unlike the late afternoon (1800 LST) from satellites (Figures 4, 6, and 8). Nor can the model simulate the vertical phase propagation of high clouds with time well. The strong vertical phase lag revealed by observations is much weaker in AM2/LM2. For example, observations show that the phase lag between clouds with tops at 210 K and clouds with tops at 250 K is about 12 hours. However, this phase lag in AM2/LM2 is only about 6 hours.

[41] AM2/LM2 also performs poorly in simulating the diurnal cycle of UTH over the oceans. First, the simulated diurnal phase is about 6 hours later than observed, that is, the simulated oceanic UTH peaks in the early morning (0600 LST) (Figures 5, 7, and 10) in contrast to the midnight (0000 LST) observed from satellites (Figures 4, 6, and 8). Second, the diurnal magnitude as well as its relative magnitude are severely underestimated in AM2/LM2, only about 25–50% of the observed values, especially in the oceanic deep convective regions. Third, similar to land, AM2/LM2 severely underestimates the diurnal cycle of very high UTH (>80%) as discussed earlier.

[42] Clearly, AM2/LM2 still has considerable difficulties in capturing both the diurnal phases and magnitudes of UTH, high clouds, and convection over ocean. It is interesting to note that the diurnal cycle of oceanic precipitation closely follows the diurnal cycle of CAC instead of DCC (Figures 7 and 10), implying that the model's oceanic precipitation may be mainly generated by CAC instead of DCC as observed from satellites [e.g., *Fu et al.*, 1990; *Janowiak et al.*, 1994; *Chen and Houze*, 1997] (see section 2.1). Furthermore, the observed large diurnal phase lag between UTH, high clouds, and precipitation cannot be reproduced by AM2/LM2. This is clearly demonstrated by the close diurnal cycle between UTH, high-cloud amount, and precipitation as shown in Figure 10.

[43] Similar to land, the poor performance of AM2/LM2 in the diurnal cycle simulation over the oceans suggests that there may exist some important deficiencies in the model's convection and cloud parameterization schemes. For example, the cloud and moisture adjustment timescale in the model convection parameterization may be too short and the model grid size may be too large for the model to be able to represent the gradual growth and decay of the mesoscale convective systems as described by *Chen and Houze* [1997]. As a result, the diurnal phase lag between UTH, CAC, and DCC cannot be reproduced by AM2/LM2. In addition, it is interesting to note that the diurnal cycle simulation in AM2/LM2 is much worse over ocean than over land. Since the diurnal cycle of the land surface temperature is well simulated in AM2/LM2, but the model uses a fixed SST boundary condition without a diurnal cycle, it is very natural to speculate that the lack of a diurnally varying SST is mainly responsible for the worse diurnal cycle simulation over ocean. In fact, as argued by *Chen and Houze* [1997], the diurnally varying SST is instrumental to the oceanic diurnal cycle, especially the diurnal phase; that is, the diurnal heating of the ocean surface during the day provides a preferred starting time for convective systems in the afternoon. Because AM2/LM2 does not have a diurnally varying SST, the preferred afternoon initiation of new convective systems may no longer exist in AM2/LM2, and thus may affect the diurnal phase and amplitude of the convective cloud systems in the model. However, it is also possible that the worse diurnal cycle simulation over ocean is only a result of the model's physical parameterization deficiencies because the oceanic diurnal cycle is mainly regulated by the radiation-convection-dynamics interaction instead of surface temperature over land as proposed by *Gray and Jacobson* [1977] and *Randall et al.* [1991]. Over land, due to the dominance of the strong diurnal cycle of the land surface temperature, these deficiencies have a relatively small impact on the simulated diurnal cycle. In contrast, these deficiencies will dominate the simulated diurnal cycle over ocean and therefore cause a worse diurnal cycle simulation over ocean than over land if the hypotheses of *Gray and Jacobson* [1977] and *Randall et al.* [1991] are valid. Thus it is very important to further investigate the reasons for the poor diurnal cycle simulation over the oceans. Not only will this help us to validate the model's cloud and convection parameterization schemes, but also help us to understand the physical mechanisms behind the oceanic diurnal variations. Nevertheless, the poor diurnal cycle simulation over ocean (worse than over land) in AM2/LM2 suggests that the lack of a diurnal cycle in SST may be a shortcoming in the boundary forcing for atmosphere GCMs.

5. Summary and Conclusions

[44] Many studies have demonstrated that comparisons of the diurnal cycle between observations and a GCM represent a powerful tool for assessing and evaluating the GCM performance [e.g., *Slingo et al.*, 1987; *Randall et al.*, 1991; *Lin et al.*, 2000; *Yang and Slingo*, 2001; *Betts and Jakob*, 2002; *Dai and Trenberth*, 2004]. Furthermore, the diurnal cycle of tropical UTH is poorly documented despite many studies on the diurnal cycle in the tropical hydrological

cycle. Motivated by these two points, this study documents the diurnal cycle of UTH and its relationship to deep convection and high clouds in the whole tropics, and evaluates the ability of the new GFDL AM2/LM2 to simulate these diurnal variations, relying on a new data set constructed from global, high-resolution (3-hourly, $0.1° \times 0.1°$ longitude-latitude) water vapor (6.7 μm) and window (11 μm) radiances from multiple geostationary satellites.

[45] The diurnal cycle in deep convection/precipitation/ DCC and high clouds (mainly CAC) based on these satellite data generally agrees with previous observational studies [e.g., *Gray and Jacobson*, 1977; *Dai*, 2001; *Hendon and Woodberry*, 1993; *Janowiak et al.*, 1994; *Chen and Houze*, 1997; *Soden*, 2000; *Yang and Slingo*, 2001; *Imaoka and Spencer*, 2000; *Nesbitt and Zipser*, 2003]. Large diurnal variations in deep convection/precipitation and high clouds are observed over the deep convective regions, where the daily mean precipitation and high-cloud amount are abundant. The diurnal cycle in high clouds and deep convection features a clear land-sea contrast. Over land, the diurnal variation of deep convection/precipitation is stronger (around 4–10 mm day^{-1}, comparable to its daily mean), and maximum deep convection/precipitation occurs in the late afternoon and early evening (1700–2200 LST). In contrast, it is relatively weaker (around 1–3 mm day^{-1}, only about 20% of its daily mean) over ocean, and the oceanic deep convection/precipitation tends to peak around early morning (0600–0900 LST). The diurnal variation of high clouds is also stronger (around 10%, about half of its daily mean) over land, and typically peaks in the late evening (2000–2400 LST). However, it is relatively small (around 4%, about 10% of its daily mean) over ocean, and typically peaks in the late afternoon (1500–1800 LST) [e.g., *Udelhofen and Hartmann*, 1995; *Bergman and Salby*, 1996; *Soden*, 2000]. Over land, the diurnal cycle of the convective cloud systems can be mainly attributed to a direct thermodynamic response to the strong diurnal cycle of the land surface temperature [*Wallace*, 1975]. On the other hand, the physical mechanisms behind the diurnal cycle of oceanic convective clouds remain poorly understood, and are still a subject of intense research. Several hypotheses have been proposed, such as the daily variation of the differential radiative heating between the convective and cloud-free regions [e.g., *Gray and Jacobson*, 1977], the stabilization of the upper troposphere by solar absorption during the day and the destabilization of the upper troposphere by the cloud-top IR cooling at night [e.g., *Randall et al.*, 1991], as well as a combined result of the diurnally varying SST and the life cycle of convective cloud systems [*Chen and Houze*, 1997].

[46] Interestingly, similar to deep convection and high clouds, coherent diurnal variations (around 6%) in UTH are also observed over the deep convective regions, where the daily mean UTH is high. In addition, the diurnal cycle in UTH also features a clear but relatively small land-sea contrast. The diurnal variation of UTH is relatively stronger (around 4–6%, about 10% of its daily mean) over land, whereas it is relatively weaker (around 2–4%, about 6% of its daily mean) over ocean. UTH, especially high UTH (>65%), generally tends to peak around 0300 LST over land in contrast to midnight (0000 LST) over the oceans. The

current diurnal phase in UTH is consistent with *Soden* [2000] based on satellite-observed $T_{6.7}$ and *Dai et al.* [2002] based on radiosonde data from the ARM CART site near Lamont, Oklahoma. There exists a distinct phase lag between UTH, high clouds, and deep convection (Figure 8). UTH lags high clouds by about 6–8 hours, and high clouds further lag deep convection by about 3–9 hours. This phase lag relationship indicates that the diurnal cycle of UTH is regulated by the diurnal cycle of deep convection and high clouds. This is also consistent with the traditional view that deep convection serves to moisten the upper troposphere through the evaporation of the CAC generated by the deep convection [e.g., *Betts*, 1990; *Sun and Lindzen*, 1993; *Soden and Fu*, 1995; *Soden*, 1998, 2000; *Held and Soden*, 2000].

[47] When compared to the satellite observations, AM2/LM2 can roughly capture the diurnal phases of precipitation, deep convection, high clouds, and UTH over land. However, the diurnal magnitudes of precipitation, deep convection, high clouds, and UTH over land are noticeably weaker in the model. Over the oceans, AM2/LM2 has several problems in simulating the diurnal variability. First, the diurnal magnitudes of UTH, high clouds, and precipitation are underestimated. Second, the high-cloud cover for a broad range of cloud-tops (210 K < T_{11} < 260 K) including DCC and CAC are nearly 12 hours out of phase with observations. Third, the diurnal cycle of precipitation closely follows the diurnal cycle of CAC instead of DCC as observed from satellites [e.g., *Fu et al.*, 1990; *Janowiak et al.*, 1994; *Chen and Houze*, 1997]. Fourth, the observed diurnal phase lag between UTH, high clouds, and precipitation cannot be reproduced by AM2/LM2. These results reveal some important deficiencies in the model's convection and cloud parameterization schemes related to the triggering of deep convection and its life cycle. Furthermore, the weakness of the simulated diurnal cycle over the oceans compared to that over land suggests that the lack of a diurnal cycle in SST may be a shortcoming in the boundary forcing for atmospheric models.

References

Albright, M. D., E. E. Recker, and R. J. Reed (1985), The diurnal variation of deep convection and inferred precipitation in the central tropical Pacific during January–February 1979, *Mon. Weather Rev.*, *113*, 1663–1680.

Arkin, P. A. (1979), The relationship between fractional coverage of high clouds and rainfall accumulations during GATE over the B-scale array, *Mon. Weather Rev.*, *107*, 1382–1387.

Arkin, P. A., and B. N. Meisner (1987), The relationship between large-scale convective rainfall and cold cloud over the western hemisphere during 1982–84, *Mon. Weather Rev.*, *115*, 51–74.

Bergman, J. W., and M. L. Salby (1996), Diurnal variations of cloud cover and their relationship to climatological conditions, *J. Clim.*, *9*, 2802–2820.

Betts, A. K. (1990), Greenhouse warming and the tropical water budget, *Bull. Am. Meteorol. Soc.*, *71*, 1464–1465.

Betts, A. K., and C. Jakob (2002), Evaluation of the diurnal cycle of precipitation, surface thermodynamics, and surface fluxes in the ECMWF model using LBA data, *J. Geophys. Res.*, *107*(D20), 8045, doi:10.1029/2001JD000427.

Chang, A. T. C., L. S. Chiu, and G. Yang (1995), Diurnal cycle of oceanic precipitation from SSM/I data, *Mon. Weather Rev.*, *123*, 3371–3380.

Chen, S. S., and R. A. Houze Jr. (1997), Diurnal variation and life-cycle of deep convective systems over the tropical Pacific warm pool, *Q. J. R. Meteorol. Soc.*, *123*, 357–388.

Dai, A. (2001), Global precipitation and thunderstorm frequencies. Part II: Diurnal variations, *J. Clim.*, *14*, 1112–1128.

Dai, A., and K. E. Trenberth (2004), The diurnal cycle and its depiction in the Community Climate System Model, *J. Clim.*, *17*, 930–951.

Dai, A., J. Wang, R. H. Ware, and T. Van Hove (2002), Diurnal variation in water vapor over North America and its implications for sampling errors in radiosonde humidity, *J. Geophys. Res.*, *107*(D10), 4090, doi:10.1029/2001JD000642.

Elliot, W. P., and D. J. Gaffen (1991), On the utility of radiosonde humidity archives for climate studies, *Bull. Am. Meteorol. Soc.*, *72*, 1507–1520.

Fu, R., A. Del Genio, and W. B. Rossow (1990), Behavior of deep convective clouds in the tropical Pacific deduced from ISCCP radiances, *J. Clim.*, *3*, 1129–1152.

Garreaud, R. D., and J. M. Wallace (1997), The diurnal march of convective cloudiness over the Americas, *Mon. Weather Rev.*, *125*, 3157–3171.

Gray, W. M., and R. W. Jacobson (1977), Diurnal variation of deep cumulus convection, *Mon. Weather Rev.*, *105*, 1171–1188.

Hartmann, D. L., and E. E. Recker (1986), Diurnal variation of outgoing longwave radiation in the tropics, *J. Appl. Meteorol.*, *25*, 800–812.

Held, I. M., and B. J. Soden (2000), Water vapor feedback and global warming, *Ann. Rev. Energy Environ.*, *25*, 441–475.

Hendon, H. H., and K. Woodberry (1993), The diurnal cycle of tropical convection, *J. Geophys. Res.*, *98*, 16,623–16,637.

Imaoka, K., and R. W. Spencer (2000), Diurnal variation of precipitation over the tropical oceans observed by TRMM/TMI combined with SSM/I, *J. Clim.*, *13*, 4149–4158.

Janowiak, J., P. A. Arkin, and M. Morrissey (1994), An examination of the diurnal cycle in oceanic tropical rainfall using satellite and in situ data, *Mon. Weather Rev.*, *122*, 2296–2311.

Lin, X., D. A. Randall, and L. D. Fowler (2000), Diurnal variability of the hydrologic cycle and radiative fluxes: Comparisons between observations and a GCM, *J. Clim.*, *13*, 4159–4179.

Mapes, B. E., and R. A. Houze Jr. (1993), Cloud clusters and superclusters over the oceanic warm pool, *Mon. Weather Rev.*, *121*, 1398–1415.

Moorthi, S., and M. J. Suarez (1992), Relaxed Arakawa-Schubert: A parameterization of moist convection for general circulation models, *Mon. Weather Rev.*, *120*, 978–1002.

Morcrette, J.-J. (1991), Evaluation of model-generated cloudiness: Satellite-observed and model-generated diurnal variability of brightness temperature, *Mon. Weather Rev.*, *119*, 1205–1224.

Nesbitt, S. W., and E. J. Zipser (2003), The diurnal cycle of rainfall and convective intensity according to three years of TRMM measurements, *J. Clim.*, *16*, 1456–1475.

Randall, D. A., Harshvardhan, and D. A. Dazlich (1991), Diurnal variability of the hydrologic cycle in a general circulation model, *J. Atmos. Sci.*, *48*, 40–62.

Reynolds, R. W., N. A. Rayner, T. A. Smith, D. C. Stokes, and W. Wang (2002), An improved in situ and satellite SST analysis for climate, *J. Clim.*, *13*, 1609–1625.

Rotstayn, L. (1997), A physically based scheme for the treatment of stratiform clouds and precipitation in large-scale models. I: Description and evaluation of the microphysical processes, *Q. J. R. Meteorol. Soc.*, *123*, 1227–1282.

Rozendaal, M. A., C. B. Leovy, and S. A. Klein (1995), An observational study of diurnal variations of marine stratiform cloud, *J. Clim.*, *8*, 1795–1809.

Slingo, A., R. C. Wilderspin, and S. J. Brentnall (1987), Simulations of the diurnal cycle of outgoing longwave radiation with an atmospheric GCM, *Mon. Weather Rev.*, *115*, 1451–1457.

Smith, G. L., and D. A. Rutan (2003), The diurnal cycle of outgoing long-wave radiation from Earth Radiation Budget Experiment measurement, *J. Atmos. Sci.*, *60*, 1529–1542.

Soden, B. J. (1998), Tracking upper tropospheric water vapor radiances: A satellite perspective, *J. Geophys. Res.*, *103*, 17,069–17,081.

Soden, B. J. (2000), The diurnal cycle of convection, clouds, and water vapor in the tropical upper troposphere, *Geophys. Res. Lett.*, *27*, 2173–2176.

Soden, B. J., and F. P. Bretherton (1993), Upper tropospheric relative humidity from the GOES 6.7 μm channel: Method and climatology for July 1987, *J. Geophys. Res.*, *98*, 16,669–16,688.

Soden, B. J., and F. P. Bretherton (1996), Interpretation of TOVS water vapor radiances in terms of layer average relative humidities: Method and climatology for the upper, middle and lower troposphere, *J. Geophys. Res.*, *101*, 9333–9343.

Soden, B. J., and R. Fu (1995), A satellite analysis of deep convection, upper tropospheric humidity and the greenhouse effect, *J. Clim.*, *8*, 2333–2351.

Soden, B. J., et al. (2000), An intercomparison of radiation codes for retrieving upper tropospheric water vapor in the 6.3 μm band, *Bull. Am. Meteorol. Soc.*, *81*, 797–808.

Soden, B. J., D. D. Turner, B. M. Lesht, and L. M. Miloshevich (2004), An analysis of satellite, radiosonde, and lidar observations of upper tropospheric water vapor from the ARM Program, *J. Geophys. Res.*, *109*, D04105, doi:10.1029/2003JD003828.

Stuart-Menteth, A. C., I. S. Robinson, and P. G. Challenor (2003), A global study of diurnal warming using satellite-derived sea surface temperature, *J. Geophys. Res.*, *108*(C5), 3155, doi:10.1029/2002JC001534.

Sun, D.-Z., and R. S. Lindzen (1993), Distribution of tropical tropospheric water vapor, *J. Atmos. Sci.*, *50*, 1643–1660.

Tiedtke, M. (1993), Representation of clouds in large-scale models, *Mon. Weather Rev.*, *121*, 3040–3061.

Udelhofen, P. M., and D. L. Hartmann (1995), Influence of tropical cloud systems on the relative humidity in the upper troposphere, *J. Geophys. Res.*, *100*, 7423–7440.

Wallace, J. M. (1975), Diurnal variations in precipitation and thunderstorm frequency over the conterminous United States, *Mon. Weather Rev.*, *103*, 406–419.

Webster, P. J., C. A. Clayson, and J. A. Curry (1996), Clouds, radiation and the diurnal cycle of sea surface temperature in the tropical western Pacific Ocean, *J. Clim.*, *9*, 1712–1730.

Wilcox, E. M. (2003), Spatial and temporal scales of precipitating tropical cloud systems in satellite imagery and the NCAR CCM3, *J. Clim.*, *16*, 3545–3559.

Xie, P., and P. A. Arkin (1997), Global precipitation: A 17-year monthly analysis based on gauge observations, satellite estimates, and numerical model outputs, *Bull. Am. Meteorol. Soc.*, *78*, 2539–2558.

Yang, G.-Y., and J. M. Slingo (2001), The diurnal cycle in the tropics, *Mon. Weather Rev.*, *129*, 784–801.

————————————

B. J. Soden, NOAA Geophysical Fluid Dynamics Laboratory, Forrestal Campus, U.S. Route 1, Princeton, NJ 08542, USA.

B. Tian, Atmospheric and Oceanic Sciences Program, Princeton University, PO Box 308, Princeton, NJ 08542, USA. (baijun.tian@noaa.gov)

X. Wu, NOAA/NESDIS Office of Research and Application, NOAA/NESDIS/ORA E/RA1, Room 7214, 5200 Auth Road, Camp Springs, MD 20746-4304, USA.